Measurements and modeling of the microwave impedance in high-T_c grain-boundary Josephson junctions: Fluxon generation and rf Josephson-vortex dynamics

Y. M. Habib
Department of Physics, Massachusetts Institute of Technology, Cambridge, Massachusetts 02139-4307; Lincoln Laboratory, Massachusetts Institute of Technology, Lexington, Massachusetts 02173-9108; and Rome Laboratory, Hanscom AFB, Bedford, Massachusetts 01731-3010

C. J. Lehner* and D. E. Oates
Lincoln Laboratory, Massachusetts Institute of Technology, Lexington, Massachusetts 02173-9108 and Department of Physics, Massachusetts Institute of Technology, Cambridge, Massachusetts 02139-4307

L. R. Vale and R. H. Ono
National Institute of Standards and Technology, Boulder, Colorado 80303

G. Dresselhaus
Francis Bitter Magnet Laboratory, Massachusetts Institute of Technology, Cambridge, Massachusetts 02139-4307 and Rome Laboratory, Hanscom AFB, Bedford, Massachusetts 01731-3010

M. S. Dresselhaus
Department of Physics and Department of Electrical Engineering and Computer Science, Massachusetts Institute of Technology, Cambridge, Massachusetts 02139-4307

(Received 3 December 1997)

Measurements and modeling of the microwave-frequency (rf) power dependence of the impedance in Y-Ba-Cu-O thin-film grain-boundary Josephson junctions (JJ's) are presented. Microwave impedance measurements were performed using a stripline resonator with an engineered grain-boundary JJ as a function of rf current (10^{-4}–1 A) and temperature (5–70 K). To understand the observed power dependence, we have developed a long-junction model which allows for Josephson-vortex creation, annihilation, and motion. The impedance calculated using the long-junction model fits the measured data qualitatively. We show that Josephson vortices generated by the rf fields cause nonlinearities in the impedance, resulting in increases in both resistance and reactance with steps in the resistance due to flux quantization. These observations and analysis of Josephson-vortex effects at microwave frequencies have important implications for understanding rf power handling in high-T_c films. [S0163-1829(98)04621-9]

I. INTRODUCTION

Josephson-junction (JJ) effects in high-T_c superconducting thin films at microwave frequencies are a source of power loss. The nucleation and motion of Josephson vortices by microwave currents has been proposed as a cause of nonlinearities in the surface impedance.[1] We are studying the rf power dependence of engineered Y-Ba-Cu-O grain-boundary JJ's to further the fundamental understanding of the physics governing Josephson effects and loss mechanisms in high-T_c films. This study provides evidence for the observation and quantification of the power losses associated with Josephson-vortex creation and annihilation by rf currents.

The rf surface impedance, $Z_s = R_s + iX_s$, in high-T_c thin-film superconductors is linear at low power levels but becomes nonlinear at higher powers.[2] Nonlinearities limit power-handling capabilities, and hence, limit possible device applications. The power dependence has been attributed to defect structures within the superconducting material.[3] While the morphology and distribution of these defects vary greatly from film to film,[3] the observed granular nature of the films has led to a coupled-grain model for the measured surface impedance as a function of rf current, which in many cases has yielded good agreement with experiment.[2,4–6] In this coupled-grain model, the superconducting film is modeled by many ideal superconducting grains that are separated by grain-boundary weak links, thus forming a random network of coupled Josephson junctions with a distribution of properties. A systematic study of the microwave power-handling capabilities of engineered high-T_c grain-boundary JJ's is useful for interpreting the observed rf power dependence of thin films within the context of a coupled-grain model. Understanding these extrinsic loss mechanisms could lead to the production of films with greater power-handling capabilities.

In this paper, we report on measurements and modeling of the power-dependent rf impedance of grain-boundary JJ's engineered by growing high-quality Y-Ba-Cu-O films on sapphire bicrystal substrates. This comprehensive study quantifies many of the rf power-handling properties of grain-boundary JJ's. Microwave measurements are performed using a stripline resonator technique which allows us to distinguish the electrodynamic characteristics of the JJ from the rest of the film in the resonator structure. The measured resistance and reactance as a function of rf current are pre-

sented and the measured data are fit using a long-junction model that we have developed to simulate solutions of the sine-Gordon equation while imposing the unique input conditions associated with the current distribution in the stripline resonator. This model provides a means to examine the mechanism of fluxon nucleation and the dynamics of Josephson vortices generated by rf currents in the grain-boundary JJ. Analysis of the measured and modeled data specifically shows that Josephson vortices created by rf currents cause nonlinearities in the impedance.

This paper is organized as follows: in Sec. II, we present our experimental technique and show the results of rf and dc measurements. In Sec. III, we introduce the extended resistively shunted junction (ERSJ) model that we have developed to investigate long-junction effects at microwave frequencies. In Sec. IV, we compare the results of the measurements with the modeling. In Sec. V, we explain how fluxon nucleation in the grain-boundary JJ by rf currents creates Josephson vortices and how these vortices affect the rf impedance.

II. EXPERIMENTAL TECHNIQUE

A. Device preparation

The grain-boundary junctions used in this study were fabricated by growing 1400-Å-thick, epitaxial, c-axis-oriented $YBa_2Cu_3O_{7-\delta}$ (YBCO) films on 1-cm by 1-cm r-plane (1012) commercially obtained sapphire bicrystal substrates with a 24°-misorientation angle. Sapphire is a useful substrate for microwave applications due to its relatively small dielectric constant ($\epsilon \approx 9$) and low loss tangent ($\tan\delta < 10^{-7}$). The film was grown by pulsed-laser deposition (PLD) after an epitaxial buffer layer of CeO_2 was deposited on the bicrystal substrate as has been described in detail elsewhere.[7]

After YBCO deposition, the film was patterned using standard photolithographic techniques and was etched using a 0.25% phosphoric acid solution. On a single bicrystal substrate we pattern both a resonator line to be used for rf measurements and a four-point test structure for performing critical-temperature T_c and dc current-voltage I-V measurements. Since both the rf and dc measurements are performed on lines patterned from a film grown on a single substrate, we expect the separate test structures to have similar physical characteristics. The width of the lines, which corresponds to the length of the JJ, is 150 μm in both cases. Once the dc measurements were completed, the dc test structure was removed by etching so that it did not electrically couple to the resonator line during rf measurements. Such a coupling could produce spurious resonances or could lower the Q of the designed resonances. The dc measurements require silver electrical contacts to be deposited on the YBCO and therefore cannot be done on the resonator line used for the rf measurements. The resonator line is shown schematically in Fig. 1. This structure is packaged with 1400-Å-thick YBCO-on-sapphire ground planes on either side to prevent radiative losses. This results in the standard stripline-resonator structure. Two of the above-mentioned devices were prepared for this study and dc measurements performed on both showed similar results. The rf measurements were performed on one of these devices and all data presented here are for that device.

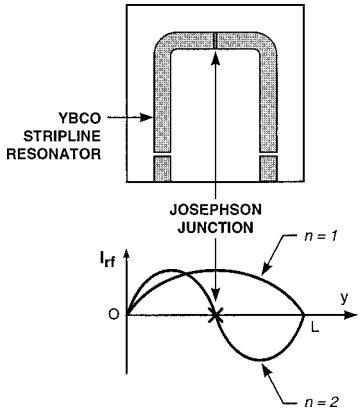

FIG. 1. The upper figure shows the patterned YBCO stripline resonator used in this study. The schematic includes the capacitive coupling strips at the resonator ends. The width of the line is 150 μm with a film thickness of 1400 Å. The grain-boundary junction is positioned at the midpoint of the stripline as shown. The lower figure shows the rf current distribution $I_{rf}(x)$ along the length L of the stripline for the standing waves of the first two resonant modes. The first ($n=1$) mode has a current peak at the junction, while the second ($n=2$) mode has a current node at the position of the JJ.

B. dc measurements

The dc measurements were performed on the test structures discussed above using standard four-point techniques. Measurement of the resistive T_c showed a midpoint transition of 89.6 K and a 10–90 % transition width of approximately 2 K.

We performed I-V measurements from 5 to 80 K to obtain the Josephson critical current I_c and the normal-channel resistance R_n as a function of temperature. In Fig. 2 we show the temperature dependence of I_c with a typical I-V curve ($T=40$ K), from which the I_c and R_n data were extracted shown in the inset. I-V curves, such as the one in the inset in Fig. 2, were taken at each temperature shown by the data points. The R_n remained constant over the entire temperature range with a value of $R_n = 80 \pm 10$ mΩ. Films from the same laser deposition grown on single-crystal sapphire substrates had a critical current about three orders of magnitude greater than those grown on bicrystal substrates. The I-V curves show no hysteresis which is typical of RSJ-like, overdamped junctions.[8] The I-V curves also show no evidence for flux-flow rounding at the resistive transition. We also note that these grain-boundary junctions show a large excess current, $I_{ex} = I - V/R_n \approx I_c$, which has also been reported by other researchers in similar systems.[9,10] The measured critical current is very sensitive to magnetic fields and hence magnetic shielding was used to ensure an ambient field $B < 10^{-7}$ T in the sample-measurement space for all measurements reported here.

C. rf measurements

We have developed a stripline resonator configuration with an engineered JJ which allows us to distinguish the rf

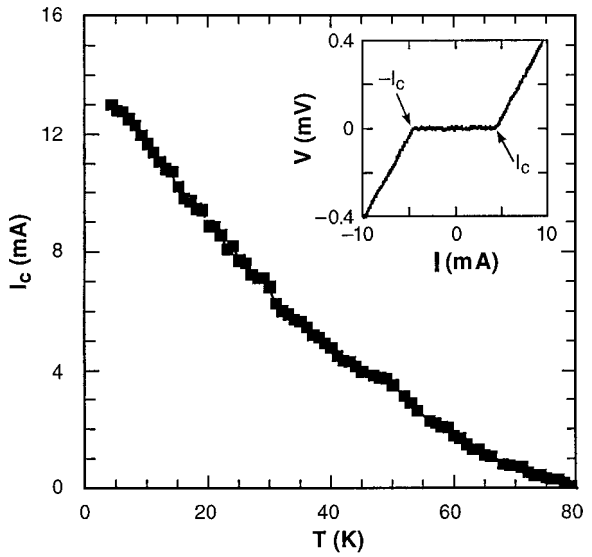

FIG. 2. Measured temperature dependence of the junction critical current I_c. The inset is a typical I-V curve measured at 40 K from which the I_c and R_n at each temperature were determined. All the observed temperature dependence was in I_c, with R_n remaining temperature independent, $R_n \approx 80\ \text{m}\Omega \pm 10\ \text{m}\Omega$.

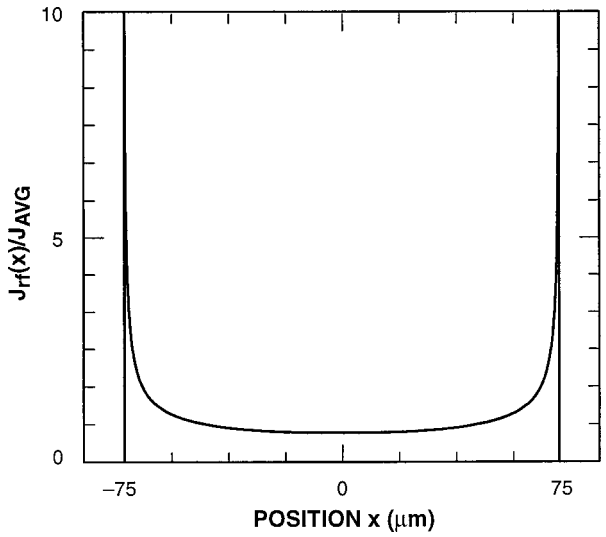

FIG. 3. The current density distribution in the stripline showing the normalized current density $J_{\text{rf}}(x)/J_{\text{AVG}}$ as a function of position x across the width ($w = 150\mu\text{m}$) of the stripline. The current density is peaked at the edges of the line and is approximately ten times greater at the edges than at the center. The current density is uniform through the thickness of the film.

power-handling properties of the JJ from those of the rest of the film. Our experimental technique has been previously employed for measurements on superconducting–normal-metal–superconducting (SNS) ramp junctions.[11,12] The resonator structure is patterned such that the grain-boundary JJ is positioned precisely at the midpoint of the stripline length $L \approx 2$ cm and spanning the entire width as shown in the upper part of Fig. 1. The resonant frequency of the fundamental mode is $f_1 = 3.0$ GHz with overtone resonant modes at $f_n \approx n f_1$ where n is an integer. At resonance, the fundamental $n = 1$ mode is a half-wavelength standing wave with a current maximum at the midpoint of the resonator line, where the fabricated JJ is positioned. In contrast, the $n = 2$ mode is a full-wavelength standing wave with a current node at the position of the JJ. Thus, the $n = 1$ mode will be maximally affected by the JJ, while the $n = 2$ mode will be minimally affected. The current distributions along the length of the stripline for the first two modes are shown in the lower part of Fig. 1. Comparing the measured results on these two modes is the method we employ to separate the rf properties of the engineered grain-boundary JJ from those of the remainder of the superconducting film constituting the majority of the resonator structure.

Microwave measurements were performed on the resonator for the first two modes as a function of input power and temperature. The measurements were carried out using a vector network analyzer with post-device and predevice amplifiers to facilitate measurement over an input power range from 0.1 nW to 1 W. The temperature was controlled using a canister cryostat immersed in a magnetically shielded liquid-helium dewar. Temperature stability of one part in 10^3 was consistently achieved over the entire measurement range. The experimental procedure in this study directly measures the quality factor Q, the resonant frequency f_n, and the insertion loss IL, of the resonator as a function of the rf input power. From these measurements we calculate the peak rf current in the standing waves[13]

$$I_0 = \sqrt{\frac{r_v(1-r_v)4Q_u P}{n\pi Z_0}}, \tag{1}$$

where r_v is the voltage insertion ratio, which is related to the IL by $IL = -20 \log_{10} r_v$, while Q_u denotes the unloaded Q. The input power to the resonator is given by P, while n is the resonant mode number, and $Z_0 = 50\ \Omega$ is the characteristic impedance of the stripline. The rf current distribution as a function of position y along the length L of the stripline is $I_{\text{rf}}(y,t) = I_0 \sin(n\pi y/L)\cos(\omega t)$ where ω is the angular frequency of the rf signal.

We also must consider the current distribution across the width of the line and through the thickness of the film. The width w of the patterned stripline $w = 150\ \mu$m is large compared with the London penetration depth, $\lambda_l \approx 0.2\ \mu$m (at $T \leqslant 70$ K), while the thickness t of the film $t = 0.14\ \mu$m is less than λ_l, so that $w \gg \lambda_l > t$. Thus, the current density is essentially uniform through the thickness of the film, but very nonuniform across the width of the line. The normalized current density as a function of position x across the stripline width $J(x)/J_{\text{AVG}}$ is shown in Fig. 3, which was calculated using the method of Sheen *et al.*[14] The current is peaked at the edges of the line with an edge value approximately ten times greater than at the center of the line. The JJ is considered a small perturbation to the overall current distribution in the stripline structure, since the Q remains over 10^3 even at high rf current levels. We expect the JJ to have essentially no effect on the measured properties of the resonator in the low-power limit, when the current density at the stripline edges is much less than the JJ critical-current density J_c. As the input power is increased, a level P_c is reached where the rf current density in the stripline first begins to exceed the J_c of the JJ at the edges of the line. At power levels above P_c, we expect to observe JJ effects on the $n = 1$ mode measurements but we do not expect such JJ effects to influence the $n = 2$ mode data.

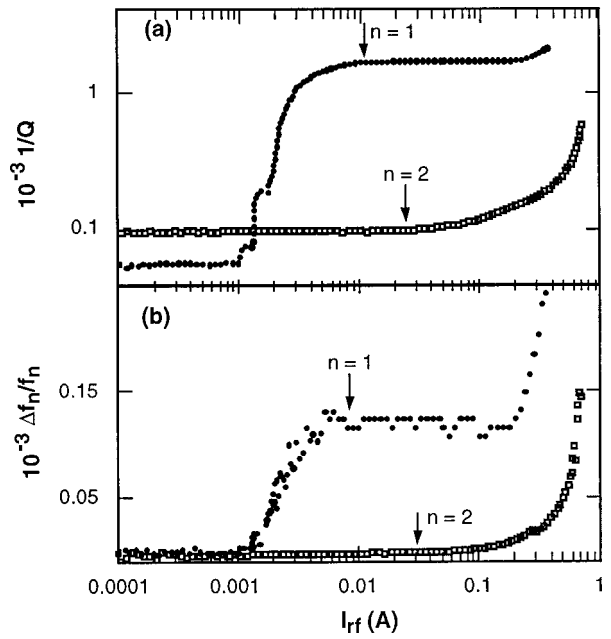

FIG. 4. This figure shows (a) the measured $1/Q$ and (b) $\Delta f_n/f_n$ data as a function of rf current for the first two [$n=1$ (filled circles) and $n=2$ (open squares)] resonant modes at 50 K. Notice that both $1/Q$ and $\Delta f_n/f_n$ rise sharply at $I_{rf}\approx 1$ mA for the $n=1$ resonant mode, while both $1/Q$ and $\Delta f_n/f_n$ for the $n=2$ mode remain almost constant for nearly two more orders of magnitude of current increase. In the range 1 mA $<I_{rf}<$ 200 mA the $n=1$ mode data are dominated by the effect of the JJ. The data for the $n=2$ mode is similar to that seen in resonators without fabricated JJ's. Also notice the steplike structures in the $1/Q$ data for the $n=1$ mode which we show to be related to fluxon nucleation.

To demonstrate the effectiveness of our experimental technique, in Fig. 4 we compare the normalized frequency shift $\Delta f_n/f_n$ (which is proportional to the reactance) and the inverse quality factor $1/Q$ (which is proportional to the resistance) as a function of rf current at 50 K for both the $n=1$ and $n=2$ modes. In the small current limit, 0.1 mA $<I_{rf}<$ 1 mA, before the onset of the JJ effects, the $\Delta f_n/f_n$ data are relatively constant (independent of I_{rf}) and nearly zero for both modes, and the $1/Q$ data are also nearly constant vs I_{rf} but with an f^2 (factor of 4) difference separating the measured values of the two modes. This low-power f^2 dependence is predicted by the two-fluid model and has been observed by many researchers.[15] At $I_{rf}\approx 1$ mA, both the $\Delta f_n/f_n$ and $1/Q$ data rise sharply for the $n=1$ mode. In contrast, the $n=2$ mode data still remains constant at $I_{rf}\approx 1$ mA, and remains so for almost two more orders of magnitude of rf current increase. The significant rise in the $\Delta f_n/f_n$ and $1/Q$ data for the $n=1$ mode at rf current levels where the $n=2$ mode remains constant is due to the JJ. When the current is increased to $I_{rf}\approx 8$ mA, the $n=1$ mode $\Delta f_n/f_n$ and $1/Q$ data become constant in current because the entire junction has reached a normal resistive state. The $1/Q$ data is used to calculate the effective JJ resistance in Sec. IV which shows the saturation value to be R_n. Once the saturation is reached, JJ effects can no longer change the values of $\Delta f_n/f_n$ and $1/Q$. In the high-current limits the $n=1$ mode $\Delta f_n/f_n$ and $1/Q$ data curve upward at $I_{rf}\approx 200$ mA which is due to effects in the superconducting film separate from the JJ. The $n=2$ mode data begin increasing at $I_{rf}\approx 100$ mA and turn sharply at $I_{rf}\approx 400$ mA and this also is attributed to losses in the superconducting film. Both the $\Delta f_n/f_n$ and $1/Q$ data change at the same values of I_{rf} for the $n=1$ and $n=2$ modes, respectively. In previous studies of YBCO films without engineered JJ's,[16] and in recent measurements we have performed on films grown by PLD on single-crystal sapphire substrates, results similar to those shown here for the $n=2$ mode were observed for all resonant frequencies. Step structures are observed in Fig. 4 in the $n=1$ mode $1/Q$ data at $I_{rf}\approx 1$ mA, which are not seen anywhere in the data for the $n=2$ mode. As we demonstrate below, the origin of these steps, and the measured sharp rise in $1/Q$ and $\Delta f_n/f_n$ for the $n=1$ mode is the nucleation of Josephson vortices in the grain-boundary JJ's by the microwave input current.

III. MODELING

The rf dynamics of a long Josephson junction are largely governed by the Josephson penetration depth λ_J, which determines the spatial extent of Josephson vortices and the inductance of the JJ. For the grain-boundary junctions used in this study, $\lambda_J=\sqrt{\Phi_0/2\pi\mu_0 J_c h_{\rm eff}}\approx 2\,\mu$m, for a typical J_c of 20 kA/cm^2 at 40 K, where Φ_0 is the flux quantum, $\Phi_0=h/2e=2.07\times 10^{-15}$ Wb, and $h_{\rm eff}$ is the effective magnetic thickness of the junction, $h_{\rm eff}=2\lambda_l+d\approx 2\lambda_l\approx 0.4\ \mu$m with d, the actual grain-boundary interlayer thickness, being negligible compared with λ_l. The width of the stripline, and therefore the length of the junction, is large compared to the Josephson penetration depth λ_J, while the thickness is small, $w\gg\lambda_J>t$, making this a long junction.[17] To properly describe the dynamics of the long junction, one needs to know how $\phi(x,t)$, the gauge-invariant phase difference of the superconducting wave function, varies in time and space. A variation in ϕ of 2π constitutes a Josephson current oscillation in time and a Josephson vortex in space. The differential equation governing the long-junction system is the sine-Gordon equation[18,19]

$$\lambda_J^2\frac{\partial^2\phi}{\partial x^2}=\sin\,\phi+\tau_J\frac{\partial\phi}{\partial t}+\tau_{RC}\tau_J\frac{\partial^2\phi}{\partial t^2}, \tag{2}$$

where $\tau_J=\Phi_0/2\pi I_c R_n$ and $\tau_{RC}=R_nC$ where C is the capacitance of the junction. For our case of an overdamped junction, the capacitive term is negligible.[18]

The rf impedance of our long junction could be calculated using solutions of Eq. (2) for $\phi(x,t)$ subject to the condition that the rf current applied to the junction has the nonuniform distribution across the width of the stripline shown in Fig. 3. Rather than analytically solving Eq. (2), we have developed an equivalent circuit model shown in Fig. 5, which simulates Eq. (2) while simultaneously imposing the appropriate input conditions. This model treats a long junction as a parallel array of one-dimensional resistively shunted junction (RSJ) circuit elements each of which is governed by the RSJ differential equation,

$$\frac{I}{I_C}=\sin\,\phi+\tau_J\frac{\partial\phi}{\partial t}, \tag{3}$$

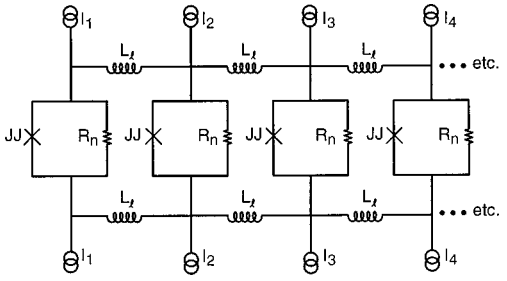

FIG. 5. The extended resistively shunted junction (ERSJ) model. In this circuit model, RSJ unit circuit elements are repeated in parallel and these unit cells are coupled by lateral inductors L_{ℓ}. Each RSJ unit has an independent current source to apply the stripline current density distribution $J_{\rm rf}(x)$ as the input to the model. In the model used to simulate a uniform junction, all the I_c, R_n, and L_{ℓ} circuit elements have the same value.

which describes the local time dependence of ϕ in each RSJ cell. To model the spatial dependence of ϕ as a continuous function over distances greater than λ_j, the individual RSJ cells in the model are coupled laterally by inductors L_{ℓ} that represent both the magnetic coupling along the JJ and the current paths through the superconducting electrodes on either side of the grain-boundary interlayer. The model employs enough RSJ unit cells (approximately 100) so that the effective spacing between adjacent cells is less than λ_J. Each of the m RSJ unit cells has a separate current source to impose the requirement that the input current distribution to the long-junction model is that of the unperturbed stripline. We refer to this model as the ERSJ model. There are three related yet adjustable parameters I_c, R_n, and L_{ℓ} that are the inputs to the model. We assign identical parameter values to all the circuit elements in the model to simulate a uniform long junction. The input parameters are related to the local values in each circuit element by, $I_c=\Sigma_{i=1}^{m} I_{ci}$, $1/R_n=\Sigma_{i=1}^{m} 1/R_{ni}$, and $L_{\ell}=\Sigma_{i=1}^{2m-2} L_{\ell i}$ for m RSJ cells. The initial values of I_c and R_n used in the model are determined by the measured dc values and are then varied by no more than a factor of 2 in fitting the measured rf data.

We obtain an initial value of the lateral inductance analytically by calculating the inductance per unit length associated with a stationary single Josephson-vortex in a long JJ. The vortex has no transport current so that the circulating vortex current I_v is conserved. In the ERSJ model, the current flowing in the x direction is through the lateral inductors, and the current flowing in the y direction passes through the RSJ unit cells, while z is the thickness through which the current does not vary. We find the lateral current $I_{vl}(x)=\int_{z=0}^{t}\int_{y=0}^{\infty} J_x dy dz=(t/\mu_0)B_z(x)$ using Ampere's law $\mu_0 J=\nabla\times B$ and integrating from the x axis to infinity. Then using the flux-phase relation $B_z(x)=(\Phi_0/2\pi h_{\rm eff})\partial\phi/\partial x$, we obtain the inductance using $\Phi=LI$ under the condition of quantization of magnetic flux from the vortex,

$$L_{\ell}=\frac{\mu_0 h_{\rm eff} w}{t}=\frac{\Phi_0}{2\pi I_c}\left(\frac{w}{\lambda_j}\right)^2\approx 10^{-10}\ \text{H} \tag{4}$$

for the total lateral inductance of this long junction. This L_{ℓ} value is the same result obtained for a parallel plate transmission line.[20] Based on this calculated value, we vary the L_{ℓ} used in the model between 10^{-10} and 10^{-11} H when fitting the measured data.

The ERSJ model is used to calculate the complex impedance of the long junction as a function of rf input current. We use JSIM,[21] a circuit-simulation program similar to SPICE, that includes small JJ circuit elements. The JSIM program calculates $\phi(t)$ at each JJ in the ERSJ circuit which we then use to calculate the voltages $V_i(t)$ and currents $I_i(t)$ of each of the circuit elements. The impedance is found by first calculating an effective voltage from the power relation for an applied rf current $I_{\rm rf}=I_a\sin\omega t$, where ω is the measured resonant frequency of the stripline device,

$$V_{\rm eff}=\frac{\Sigma_{i=1}^{m} V_i(t) I_i(t)}{I_a \sin\omega t}, \tag{5}$$

where the sum is over each circuit element in all the m individual RSJ unit cells and inductors making up the entire ERSJ model. The effective total impedance of the JJ is calculated from the $V_{\rm eff}$ in phase and out of phase with the rf current. The resistance is given by the ratio of the time average instantaneous power dissipated at the rf frequency to the time average of the current $I_{\rm RMS}$ squared,

$$R_{\rm ERSJ}=\frac{\int_0^{\tau} V_{\rm eff}(t) I_a \sin\omega t}{(I_{\rm RMS})^2 \tau}, \tag{6}$$

with τ being the period of one rf cycle. The reactance is similarly given by

$$X_{\rm ERSJ}=\frac{\int_0^{\tau} V_{\rm eff}(t) I_a \cos\omega t}{(I_{\rm RMS})^2 \tau}, \tag{7}$$

which represents the energy stored in the JJ.

IV. COMPARISON BETWEEN EXPERIMENT AND MODEL

In Sec. II C, we explained the rf measurement technique, and presented the measured $1/Q$ and frequency shift $\Delta f_n/f_n$ as a function of rf current in Fig. 4, illustrating how we directly measure rf JJ effects in the $n=1$ mode using the stripline JJ device. In Sec. III, we introduced the ERSJ model used to calculate the effective JJ resistance and reactance as a function of rf input current for a long JJ. To make a proper comparison between the power-dependence measurements on the stripline resonator and the model calculations, we obtain the effective JJ resistance from the measured Q and the reactance from the measured $\Delta f_n/f_n$ from the $n=1$ mode data as follows.

To obtain the resistance from the measured Q we first calculate the unloaded Q denoted by Q_u, which is related to the ratio of the power dissipated in the resonator to the average energy stored in it,

$$\frac{1}{Q_u}=\frac{1}{\omega}\frac{\text{Power Dissipated}}{\text{Energy Stored}}, \tag{8}$$

with ω being the resonant angular frequency of the rf signal. The resonator resistance is proportional to the power dissipated by the rf current, and hence $1/Q_u$. To obtain the effective JJ resistance from the $1/Q$ data, we consider a superconducting stripline, but represent the resistance of the fabricated JJ with a very thin piece of material of uniform resistivity ρ_n placed at the center of the line across the entire width. The power dissipated per unit volume by the rf current density J is $(1/2)\rho J^2$ for both the resistive and superconducting parts of the line. The resistivity of the superconducting line ρ_s is obtained from the complex conductivity $\sigma=\sigma_1+i\sigma_2$. At rf frequencies, we have $\rho_s \approx \sigma_1/\sigma_2^2 = 2R_s\lambda_l$, for $\sigma_1 \ll \sigma_2$. Strictly speaking, these approximations only hold for $\lambda_l \ll t$, where t is the film thickness. For the films studied in this paper $\lambda_l \approx t$ so we have $\rho_s \approx 2R_s t$. The stored energy per unit volume is $(1/2)\mu_0 H_{\rm rf}^2$, where $H_{\rm rf}$ is the rf magnetic field generated by the rf current density J in the resonator. The power dissipated and energy stored per unit volume are integrated over the length L of the stripline. With the stripline differential cross section being dA, we arrive at the following relationship:[11,15]

$$\frac{1}{Q_u}=\left[2R_s\lambda_l+\frac{2wtR_J}{L}\right]\frac{\int J^2 dA}{\omega\int \mu_0 H_{\rm rf}^2 dA}. \tag{9}$$

The first term in the brackets is proportional to the power dissipated in the superconducting line, while the second term is proportional to the power dissipated in the JJ for which we have defined an effective JJ resistance $R_J=\rho_n s/wt$ where s is the thickness of the resistive material. The ratio of the area integrals in Eq. (9) is a constant geometrical factor which can be calculated by the method of Sheen *et al.*[14]

As shown in Fig. 4, the measured $1/Q$ data for the $n=1$ mode increases by over an order of magnitude in the rf current range 1 mA $<I_{\rm rf}<$ 4 mA, while the $1/Q$ data for the $n=2$ mode remains constant. The $1/Q$ for the $n=1$ mode also saturates in the range 4 mA $<I_{\rm rf}<$ 200 mA. Both the sharp rise and the saturation of $1/Q$ are due to the grain-boundary junction. When $I_{\rm rf}<$ 1 mA, the R_s term in Eq. (9) is important, but in the current range of interest, 1 mA $<I_{\rm rf}<$ 200 mA, the R_J term in Eq. (9) dominates as Fig. 4 shows. We obtain the measured effective total JJ resistance $R_J(I_{\rm rf})$ by properly normalizing the $1/Q(I_{\rm rf})$ data on the entire grain-boundary JJ resonator structure with the coefficients of the R_J term in Eq. (9). This analysis gives the effective JJ resistance as a function of rf current,

$$R_J(I_{\rm rf})=\frac{1}{Q_u(I_{\rm rf})}\frac{L}{2wt}\frac{\omega\int \mu_0 H_{\rm rf}^2 dA}{\int J^2 dA}=\frac{\Gamma f_1}{Q_u(I_{\rm rf})} \tag{10}$$

with f_1 being the resonant frequency of the $n=1$ mode in GHz and $\Gamma=16.7\ \Omega$/GHz. This analysis allows direct comparison between the measured data and the modeling results since the JJ resistance is calculated in both cases.

We present $R_J(I_{\rm rf})$ as obtained above for a range of temperatures in Fig. 6. In the low-current limit, where R_J is approximately constant as a function of rf current, the magnitude of R_J is due to the surface resistance of the superconducting film which is strongly temperature dependent. As the current is increased, Fig. 6 shows the existence of a critical rf current value where the resistance begins to increase precipitously. The rise in R_J is due to losses in the JJ and this increase in R_J occurs at lower rf current values with increasing temperature, similar to the measured dc temperature dependence of I_c shown in Fig. 2. Step structures appear in the resistance curves above this critical rf current value. The steps are most pronounced at intermediate temperatures. As explained in more detail in Sec. V these steps result from quantization of the magnetic flux, and the sharp increases in resistance are due to Josephson vortices being created and annihilated by the rf current. As the current is further increased beyond the steps, R_J becomes independent of the rf current with all the curves saturating at essentially the same value independent of temperature: $R_J^{\rm sat}=83\ {\rm m}\Omega\pm 3\ {\rm m}\Omega$, which agrees with the measured dc R_n presented in Sec. II B.

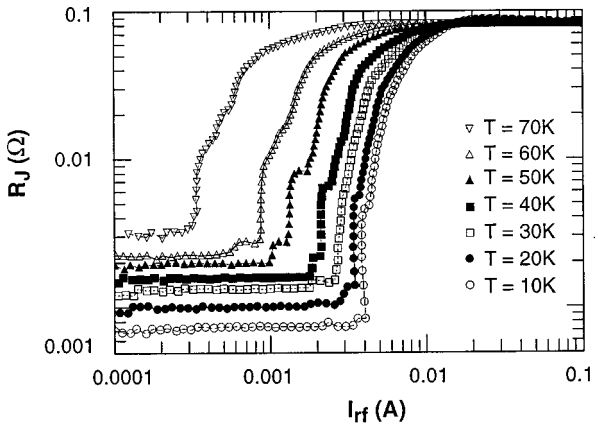

FIG. 6. The measured effective resistance, $R_J(I_{\rm rf})$ as a function of rf current presented on a log-log plot for a range of temperatures. In the low-current limit the $R_J(I_{\rm rf})$ is almost constant and is due to the surface resistance of the film, rather than to the junction. As the rf current is increased, there is a very sharp rise in the resistance curves, and step structures associated with fluxon quantization are observed. Also note that all curves saturate at the same $R_J^{\rm sat}$ whose value is about the same as the R_n obtained from the dc measurements. As T is increased, the sharp rise in R_J occurs at lower values of $I_{\rm rf}$.

We obtain the JJ reactance X_J from the measured shifts in the resonant frequency as follows. The total reactance X_T of the entire stripline JJ device is proportional to the total inductance $\mathcal{L}_T$ of the device, $X_T=\omega\mathcal{L}_T$. The resonant frequency has a functional dependence on $\mathcal{L}_T$ given by $f=1/2\pi\sqrt{\mathcal{L}_T C}$, with C, the capacitance, being a constant. From these relations we obtain

$$\frac{\Delta X_T}{X_T}=\frac{\Delta\mathcal{L}_T}{\mathcal{L}_T}=\frac{-2\Delta f}{f}. \tag{11}$$

The total inductance has three contributing terms, $\mathcal{L}_T=\mathcal{L}_g+\mathcal{L}_k+\mathcal{L}_J$ where $\mathcal{L}_g$ is the geometrical inductance of the stripline resonator, $\mathcal{L}_k$ is the kinetic inductance of the superconducting electrons, and $\mathcal{L}_J$ is the inductance due to the JJ. The $\mathcal{L}_g$ and $\mathcal{L}_k$ terms are constants as functions of rf current, so that $\Delta X_T=X_T(I_{\rm rf})-X_T(0)=X_J$. Unlike the resistance, where the contribution from the JJ is very large compared to

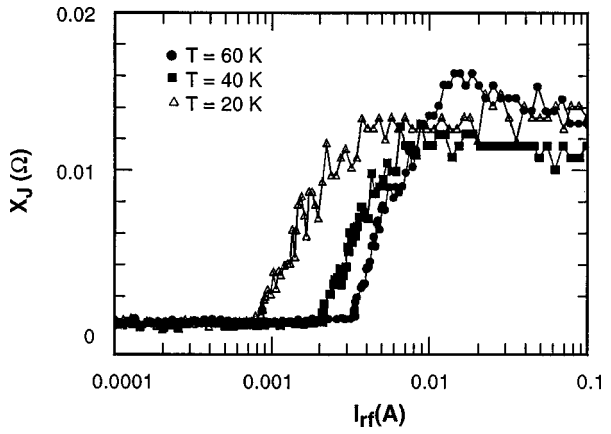

FIG. 7. The measured JJ reactance, $X_J(I_{\rm rf})$, as a function of rf current presented on a semilog plot for three different temperatures. The increase in X_J is due to an inductance increase associated with the formation of fluxons in the junction by rf currents. As T is increased, the sharp rise in $X_J(I_{\rm rf})$ occurs at lower values of $I_{\rm rf}$. For a given temperature, the rise in X_J occurs at the same value of $I_{\rm rf}$ as the R_J in Fig. 6.

the rest of the film, the reactance due to the JJ is small compared to the reactance of the rest of the film. We obtain a value for $X_T = X_g + X_k + X_J \approx X_g + X_k$, using values for $\mathcal{L}_g$ and $\mathcal{L}_k$ obtained from Sheen *et al.*[14] Hence, the JJ reactance is given by

$$X_J(I_{\rm rf}) = \frac{-2\Delta f}{f}(X_g + X_k) = \Lambda \frac{f(0) - f(I_{\rm rf})}{f(0)} \qquad (12)$$

with the geometrical factor $\Lambda = 93.2\Omega$.

The JJ reactance X_J as obtained above is shown in Fig. 7 for three different temperatures. As with the resistance shown in Fig. 6, the JJ reactance data shows the existence of a critical rf current value above which the reactance increases sharply. For a given temperature, the reactance increases occur at the same rf current level as the resistance increases with both increases being attributed to JJ dynamics. The change in reactance is attributed to the inductance change associated with fluxon generation in the grain boundary by the rf currents as explained in Sec. V. The reactance change at all temperatures in Fig. 7 is seen to rise sharply and then level off. On comparing Figs. 6 and 7, we see that the current range from the initial rise of X_J to saturation is comparable to that of R_J for a given temperature, while the magnitude of the reactance change is much smaller than that of the resistance.

In order to verify that our ERSJ model is working properly, we explored the limiting behavior by changing L_ℓ substantially from the value of 10^{-10} H obtained in Eq. (4). By making L_ℓ very small ($L_\ell \to 0$ limit) we simulate a case where $\lambda_J > w$ which is a small junction RSJ limit. In this case the ERSJ model reduces to the one-dimensional RSJ model without a current distribution. This small L_ℓ limit is identical to results obtained by solving Eq. (3) numerically for a single small junction. On the other hand, if we increase L_ℓ substantially ($L_\ell \to \infty$ limit) without decreasing the junction spacing, we obtain results identical to those obtained by solving the one-dimensional RSJ model Eq. (3) and then averaging the results over the current distribution in the stripline shown in Fig. 3. This current averaged RSJ model has been previously presented for fitting measurements on ramp-type SNS junctions.[11,12] The effect of increasing L_ℓ is to uncouple neighboring cells in the ERSJ model so that each junction is independent and lateral currents are negligible. In this case Josephson vortices are not relevant.

We show in Fig. 8 the measured JJ resistance and reactance $R_J(I_{\rm rf})$ and $X_J(I_{\rm rf})$ (points) as a function of rf current $I_{\rm rf}$ with fits from the modeling (lines) at 20 and 50 K in Figs. 8(a) and 8(b), respectively. The solid lines in Fig. 8 are the result of the ERSJ model which uses the inductance calculated in Eq. (4), while the dashed line is the model result in the $L_\ell \to \infty$ uncoupled (no vortices) limit, equivalent to the current averaged RSJ model. We define a critical rf current level I_f, the rf fluxon nucleation current where the resistance and reactance first increase abruptly, which is marked in Fig. 8 with arrows. The I_f is the rf current level that exceeds the JJ critical-current density sufficiently on the edges of the stripline that a Josephson oscillation will occur at the line edge, nucleating a fluxon, and resulting in a Josephson vortex moving into the junction. This concept is further developed in Sec. V.

Examination of the resistance plots shows step structures evident in the measured $R_J(I_{\rm rf})$ in Fig. 8 in the vicinity of I_f. There are also steps in the result of the ERSJ model when currents are allowed to redistribute and form vortices (solid lines) however, when current redistribution cannot occur ($L_\ell \to \infty$ limit), the modeling does not show steps (dashed lines). The steps in the modeled and measured data have different heights, but the overall character of the curves is qualitatively the same. The lack of quantitative agreement could be due to imperfections in the engineered junction which are not accounted for in the idealized model. The origin of the steps in the calculated $R_J(I_{\rm rf})$ curve is fluxon quantization and the increases in resistance are due to the creation, annihilation and motion of Josephson vortices as we show in Sec. V.

We compare the values of I_c and R_n obtained from the dc measurements with those obtained from the modeling by fitting the rf measurements in Table I. The same parameters were used to fit the R_J and X_J data. However, a constant R_J value below I_F is added to the model result to account for the R_S of the film. The values of R_n obtained for rf and dc are about the same. The R_n is the saturation value of the $R_J(I_{\rm rf})$ data. The I_c obtained from the rf measurements is higher than the dc value. The rf value of I_c is determined by fitting the measured data and is larger than I_f. The modeling predicts that the rf value of I_c is 4–5 times greater than I_f.

Examination of the X_J plots in Fig. 8 shows the reactance increasing sharply above I_f. This increase is attributed to the increased inductance due to Josephson fluxons nucleating in the long JJ. The ERSJ model with vortices shows the same overall features as the measured data, including a rise and then a leveling off of X_J, with the height, onset, and slope of the rise showing good agreement. On the other hand, the RSJ limit without vortices (dashed line in Fig. 8) predicts a slight decrease in $X_J(I_{\rm rf})$ above I_f, while the measurements do not show such a decrease. This agreement between the ERSJ model and the measured data adds credence to the idea that fluxons are responsible for the observed reactance, and that we are directly observing the effects of rf Josephson vortices

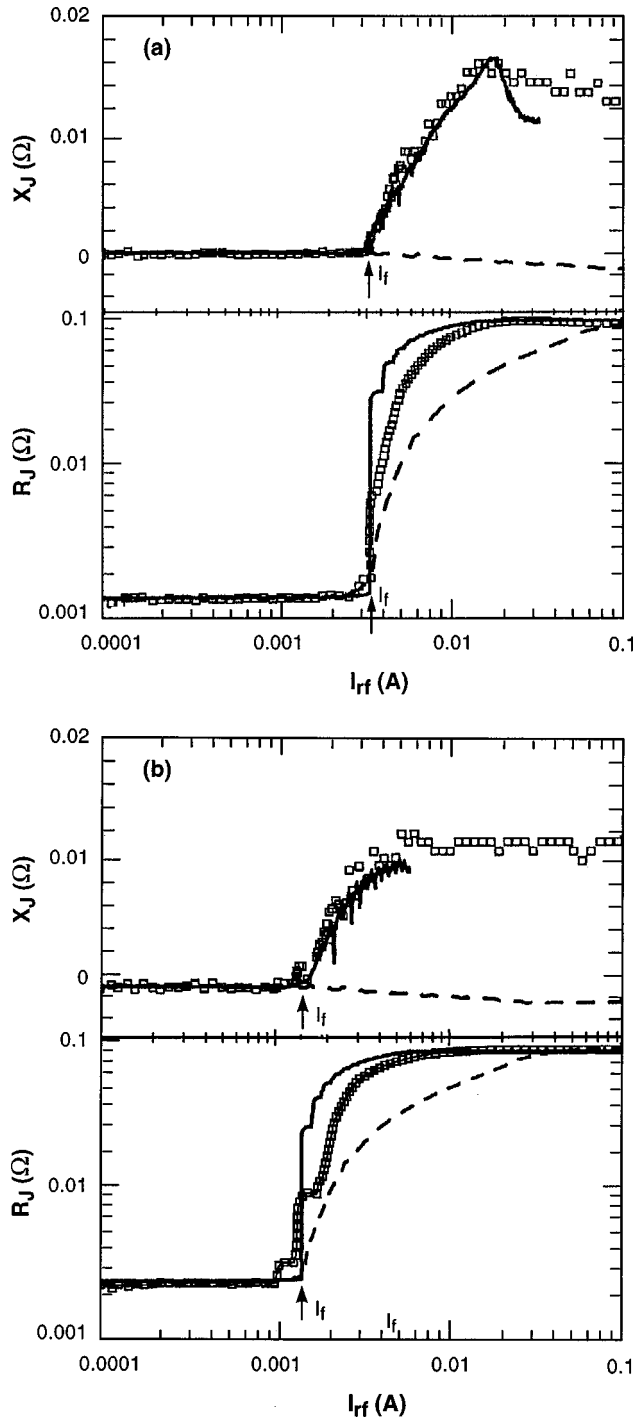

FIG. 8. Measured effective JJ resistance and reactance vs rf current, $R_J(I_{rf})$ and $X_J(I_{rf})$ (points), for the grain boundary JJ at (a) 20 and (b) 50 K compared with two fits from the modeling (lines). The solid lines are from the ERSJ model which allows for Josephson vortex formation, while the dashed lines correspond to the model in the $L_{\not}\rightarrow\infty$ limit where vortices (fluxons) play no role. The fluxon nucleation current I_f is marked with arrows in each plot. When fluxons are allowed to exist in the model stepped increases in resistance and reactance change increases occur as is also observed in the measured data.

in the measured data. The modeling is not presented over as large a current range as the data because the modeling is computationally intensive, thus limiting the number and size of the simulations that were carried out in the present work.

TABLE I. Comparison of the I_c and R_n obtained from the dc measurements and from fitting the rf measurements using the ERSJ model.

Temperature	I_c mA		R_n mΩ	
	dc	rf	dc	rf
20 K	8.9	14.0	80	81
50 K	3.5	4.8	80	86

V. FLUXON GENERATION BY RF CURRENTS AND JOSEPHSON-VORTEX DYNAMICS

As we have asserted in the previous sections, the nucleation of fluxons in the JJ is the origin of the step structures in $R_J(I_{rf})$, and of the sharp increases in $X_J(I_{rf})$ and in $R_J(I_{rf})$. Fluxon nucleation in the stripline geometry is initiated by the rf current at the edges of the junction, where the current density is greatest. When the rf input-current level to the ERSJ model is small enough to be well below I_c of the edge junctions in the circuit, all the current can flow through the JJ's and no currents flow through $L_{\not}$. As the I_{rf} to the circuit is increased to a level approaching I_c of the edge JJ's, some currents will go through $L_{\not}$ and then flow through the inner junctions. Even when the input I_{rf} is sufficient to exceed I_c of the edge JJ's, the currents can redistribute and avoid triggering a Josephson oscillation at the edge. It is when I_{rf} reaches a level that causes a Josephson current oscillation (2π phase slip) at the edges of the long junction that stepped losses and sharp increases in the resistance and reactance begin. A Josephson oscillation occurs when the current in the junction first passes through I_c and then goes back to zero (phase change of π) in one half of an rf cycle. In the pendulum model[17] of an overdamped JJ ϕ is analogous to the deflection angle θ of an overdamped pendulum which when pushed past an angle of $\theta=\pi$ will certainly fall to 2π. Similarly, once $\phi=\pi$ in the JJ, ϕ will necessarily slip another π in phase which completely nucleates a fluxon as the phase change is directly related to the flux through the junction, $\Delta\phi(t)/2\pi=\Phi(t)/\Phi_0$. Concurrent with the 2π change in ϕ, the current redistributes itself through the ERSJ circuit forming a Josephson vortex. The Josephson oscillations cause current to flow through the resistors in the RSJ cells, resulting in resistive losses. Fluxon nucleation is responsible for increases in X_J while fluxon quantization results in the steps in R_J observed at 20 K [Fig. 8(a)] and at 50 K [Fig. 8(b)].

On one edge of the JJ, when $I_{rf}\geqslant I_f$, fluxons are nucleated on the positive half of the rf cycle and antifluxons are nucleated on the negative half of the cycle. These fluxons and antifluxons correspond directly to Josephson vortices and antivortices where an antivortex has current circulating in the opposite direction to the current circulation for a vortex. When vortices meet antivortices in the junction, they annihilate each other. Power is dissipated due to normal currents when Josephson vortices are created or annihilated, with resistive losses also being attributable to the motion of vortices under the influence of the rf currents. Since the junction is overdamped, the Josephson vortices move only under the influence of the rf current. As the rf current increases, more and more Josephson vortices and antivortices move in and out of the junction. When vortices are created on one edge of

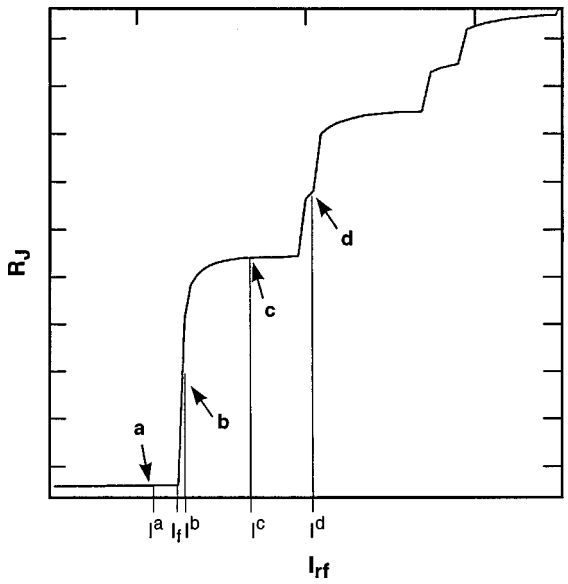

FIG. 9. Calcuated resistance as a function of rf current obtained from the ERSJ model showing stepped structures due to fluxon generation by rf currents. Four step positions are marked a, b, c, and d, each corresponding to a current I^a, I^b, I^c, and I^d. Each step is due to an additional fluxon being generated in the JJ in each rf cycle.

the JJ, antivortices are created on the opposite edge. Moreover, when the rf current is large enough to create a vortex at the edge and move it to the center of the long JJ, the vortex will meet an antivortex from the other side. A saturation level is reached where $R_J = R_n$ and X_J no longer increases with increasing $I_{\rm rf}$ as shown in Figs. 8(a) and 8(b).

We have investigated the effect of fluxon generation and the creation of Josephson vortices by rf currents in a long junction by examining sequentially the magnetic flux in the ERSJ circuit as a function of time $\Phi(t)$ (which shows fluxon nucleation) and the current distribution as a function of position $I(x)$ (which shows Josephson vortex formation). In Fig. 9, we show the $R_J(I_{\rm rf})$ which was used to fit the 20-K data in Fig. 8(a); the $R_J(I_{\rm rf})$ curve shows clear stepped structure (the plot is on a linear scale, while the fitted data in Fig. 8 are plotted on a log-log scale). Marked with arrows in Fig. 9 are four positions on the curve a, b, c, and d, which correspond to rf current levels we denote I^a, I^b, I^c and I^d. Also shown is the fluxon nucleation current I_f, which was introduced in Fig. 8. When the input current $I_{\rm rf}$ is equal to I^a, which is slightly below I_f, the magnitude of $R_J(I_{\rm rf})$ is almost constant in current and has about the same value as $R_J(I_{\rm rf} \approx 0)$. No appreciable losses have occurred in the junction at this current level. When the current is increased slightly to $I_{\rm rf} = I^b$, with $I^b = I_f + \epsilon$, it is apparent that $R_J(I_{\rm rf})$ has risen abruptly [there is a very small plateau at (b), which is not resolved in Fig. 9]. The junction is dissipating appreciable power at $I_{\rm rf} = I^b$. When the current is increased to $I_{\rm rf} = I^c$, then $R_J(I_{\rm rf})$ has further increased and reached a plateau. Finally, when $I_{\rm rf} = I^d$, the $R_J(I_{\rm rf})$ has again increased and has reached another plateau which is smaller than the one marked c in Fig. 9. As the current is further increased, steps continue to develop, alternating between smaller and larger plateaus. Each stepped increase is due to an additional fluxon nucleating in the long JJ during each rf cycle. The

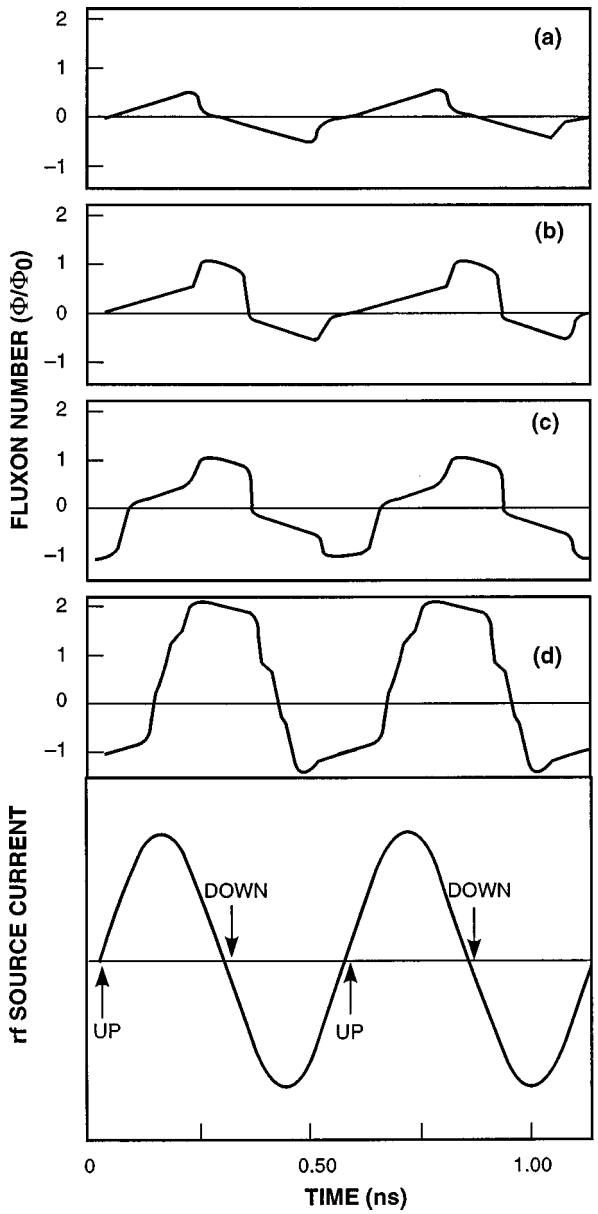

FIG. 10. Fluxon number as a function of time, $\Phi(t)/\Phi_0$, for half the long junction as calculated by the ERSJ model. The four plots (a), (b), (c), and (d) correspond to the current levels marked accordingly in Fig. 9. This figure demonstrates how the flux increases in discrete quantized units. The bottom shows the rf source current using a common time scale for the source current and the flux. Any flux present at the source current nodes is due to Josephson vortices.

plateaus correspond to ranges where the number of fluxons generated per cycle by the rf current is a constant. As we show below, the large plateaus correspond to symmetric fluxon states, while the small plateaus correspond to asymmetric fluxon states.

We show the total magnetic flux $\Phi(t)$ existing in half the ERSJ circuit (i.e., half the 150-μm-long JJ) in Fig. 10. Only half needs to be shown because the long junction is symmetric about its midpoint, as is the current distribution in the stripline. In addition, when fluxons are generated on one side of the junction, antifluxons are generated on the other side, and while the nucleation of both fluxons and antifluxons causes losses, if we calculated the total flux through the

whole junction it would sum to zero. We show four different $\Phi(t)$ plots in Figs. 10(a), 10(b), 10(c), and 10(d), with each plot showing the $\Phi(t)$ generated in the JJ by rf current levels corresponding to I^a, I^b, I^c, and I^d in Fig. 9, respectively. The $\Phi(t)$ is calculated from the ERSJ model by summing the flux due to the currents flowing in $L_{\not}$ such that $\Phi(t) = \Sigma_{i=1}^{m-1} L_{\not i} I_i(t)$, where the sum on i is over the $m-1$ inductors in half the ERSJ circuit. Shown below the $\Phi(t)$ plots in Fig. 10 is the rf source current $I_{\rm rf}(t)$ ($f=3$ GHz) on the same time scale as $\Phi(t)$. The up and down nodes in the sine wave are marked because any flux present in the junction at the nodes is due only to Josephson vortices. Figure 10(a) depicts $\Phi(t)$ for the rf current level I^a in Fig. 9 which is slightly less than I_f. A small background flux ($|\Phi| < \Phi_0/2$) is seen with the same periodicity as the source current, corresponding to a maximum phase change along the junction of just less than π, showing an incipient but not fully formed Josephson oscillation (fluxon). We note that there is no flux present [i.e., $\Phi(t)=0$] in Fig. 10(a) at the rf source current nodes which implies that the periodic flux seen is due to the source current.

When the current is increased to I^b in Fig. 9, which is a very small amount greater than the fluxon nucleation current $I^b = I_f + \epsilon$, the corresponding $\Phi(t)$ plot, Fig. 10(b), shows one fluxon nucleating in the first half of the rf cycle and then annihilating in the second half of the rf cycle. The phase in the JJ changes by 2π (one fluxon) in each half of the rf cycle, indicating that a Josephson oscillation is occurring in each half cycle. Figure 10(b) shows that there is a fluxon in the junction [$\Phi(t)=\Phi_0$] at the time of the down nodes in $I_{\rm rf}$, but the fluxon gets annihilated on the negative half of the rf cycle so that at the up node of the source current the flux is zero. We note that the nucleation occurs on the downward part of the positive rf cycle as the source current amplitude is decreasing. The nucleation and annihilation of one fluxon per rf cycle causes an abrupt and substantial increase in $R_J(I_{\rm rf})$ as shown in Fig. 9.

When we increase the current to I^c in Fig. 9 the corresponding $\Phi(t)$ plot, Fig. 10(c), shows that a fluxon nucleates and annihilates in each half of the rf cycle. Figure 10(c) shows that there is a fluxon in the junction at the time of the down nodes in the source current as in Fig. 10(b), but on the up nodes of the rf cycle an antifluxon [$\Phi(t)=-\Phi_0$] is in the junction. There are now two fully nucleated flux quanta existing in the JJ per rf cycle and consequently $R_J(I_{\rm rf})$ in Fig. 9 has increased another step.

Figure 10(d), which corresponds to the current level I^d in Fig. 9, shows two fluxons present at the down nodes of the rf source current and only one antifluxon at the up node. Each time the magnitude of $I_{\rm rf}$ increases sufficiently to add another flux quantum (fluxon or antifluxon) to the junction per rf cycle, there is a step in the $R_J(I_{\rm rf})$ in Fig. 9. The rf currents nucleate and annihilate fluxons in the long junction resulting in quantifiable losses. Note that there is no gradual increase in the flux present in the JJ at the rf nodes from one current level to the next, but only quantized increases one fluxon at a time. This type of bifurcation of phase, or equivalently flux, has been calculated by other researchers investigating similar systems.[22–24]

Figure 10 showed that fluxons can exist in the junction when the rf current is zero. The fluxons are sustained by

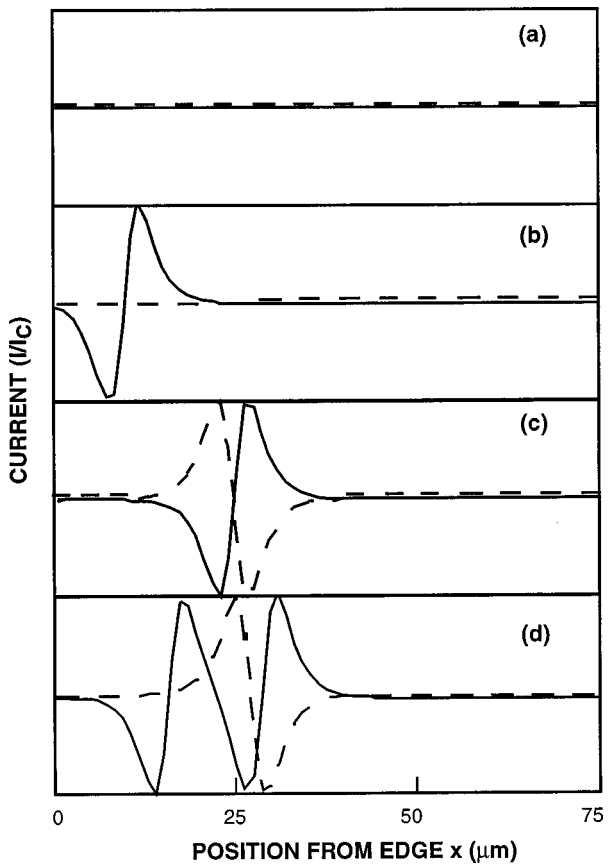

FIG. 11. Normalized current as a function of position $I(x)$ taken at the rf source current nodes shown in Fig. 10. The four plots (a), (b), (c), and (d), correspond to the current levels marked accordingly in Fig. 9. The solid lines show the current at the down nodes of the source current, while the dashed lines show the current in the junction at the up nodes of the rf source. These plots show where the Josephson vortices are located in the junction at the source current nodes and how they move farther into the JJ with increasing rf current.

circulating supercurrents that constitute Josephson vortices. In Fig. 11 we show the current $I(x,t)$ in the ERSJ circuit as a function of position x at the times when the rf source current is zero, i.e., at the nodes. We show four plots, Figs. 11(a), 11(b), 11(c), and 11(d), each corresponding to the similarly labeled current levels in Fig. 9 and the $\Phi(t)$ plots in Fig. 10. In each plot in Fig. 11 two current distributions are shown: the solid line is the current as a function of position at the down nodes of the rf source current shown in Fig. 10, while the dashed line is the current as a function of position at the up node of the rf source current. The plots in Fig. 11 show the current distribution starting at the JJ edge and extending 75 μm into the 150-μm-long junction. In Fig. 11(a) there is no current present in the junction at either of the rf source nodes. The absence of current results from the condition of zero flux at the rf nodes shown in Fig. 10(a). In Fig. 11(b) there is one vortex present in the junction. The vortex is present at the down node of the rf source current but there is no antivortex (current distribution of opposite circulation) present in the up node. Again, this follows from Fig. 10(b) that shows a fluxon present at the down nodes of the rf source but no flux at the up nodes. Figure 11(c) shows one vortex in the junction at the down nodes as in Fig. 11(b),

and also an antivortex at the up node of the rf source current. This follows from Fig. 10(c) that shows a fluxon at the down nodes and an antifluxon at the up nodes of the rf source current. In Fig. 11(d) there are now two vortices at the down node of the rf source current and one antivortex at the up node. Again this follows from the $\Phi(t)$ plot in Fig. 10(d). We note that as more vortices (or antivortices) are generated by the rf current, they move farther into the long junction as is apparent in Fig. 11.

It is interesting to examine the symmetry in Figs. 10 and 11. In Fig. 10 plots (a) and (c) are symmetric about the $\Phi(t)=0$ axis and they have the same periodicity as the rf source current, while (b) and (d) are asymmetric about this axis. This symmetry breaking is also seen in Fig. 11 where plots (a) and (c) have equal but opposite current distributions at the up and down nodes of the source current, while (b) and (d) have completely different current distributions at the up and down nodes of the source current. Since the ERSJ model and the rf source current are symmetric, these asymmetric states were unexpected. Upon further investigation of the ERSJ model results we found that the asymmetric states generate second harmonic signals. We believe that second harmonic generation is a clear indication of Josephson vortex creation by rf currents.[25]

VI. CONCLUSION

The results of the measurements and modeling presented in this paper give strong evidence that we are directly measuring the complex impedance due to fluxons being nucleated in bicrystal grain-boundary junctions. The effect of the nucleation and motion of Josephson vortices by rf currents gives rise to a nonlinear impedance, that includes step structures in the resistance, due to the quantization of the magnetic flux in the Josephson junction, and reactance changes due to the increased inductance associated with fluxon generation. The engineered JJ has very little effect on the power handling of the stripline resonator until the rf current reaches a level sufficient to nucleate the first fluxon in the JJ. Fluxon creation causes a sharp increase in the resistance and an associated rise in the reactance. As the rf current is further increased, more fluxons are generated in the junction and there is a step in the $R_J(I_{\rm rf})$ every time an additional fluxon is generated in an rf cycle. The junction then alternates between states with one more fluxon than antifluxon (asymmetric states) and those with equal numbers of fluxons and antifluxons (symmetric states) during each rf cycle. The asymmetric states produce second harmonics as a signature of the generation of Josephson vortices.

We believe that this work supports the premise that the observed nonlinear microwave power-handling effects observed in high-T_c films are due to grain-boundary weak links separating superconducting grains to form a mosaic of coupled JJ's. To the best of our knowledge this is the first direct observation and quantification of rf Josephson vortex effects in grain-boundary junctions. Recent work has shown that the nonlinearities in the high-T_c films can be explained by the coupled-grain model using a distribution of I_cR_n products in the grain boundaries.[26] Since grain-boundary weak links are an extrinsic property of the superconducting film, we believe that a further understanding of the rf electrodynamics of these structures should lead to the production of films with greater power-handling capabilities.

ACKNOWLEDGMENTS

The work at MIT (AFOSR Agreement No. F49620-95-1-0027) and at Rome Laboratory (AFOSR Agreement No. F30602-95-2-0010) was supported by AFOSR, CPT. C.J.L. was supported by the U.S. Army. The authors wish to thank R. P. Konieczka and D. Baker for lithography and other technical support, T. Weir for assistance in dc measurements, G. Fitch for computer programming, and R. Boisvert, M. Seaver, P. Murphy, and B. Reynolds of MIT Lincoln Laboratory for overall technical support. We also gratefully acknowledge numerous discussions and assistance in modeling from Dr. P. Nguyen, Dr. D. Feld, and especially Dr. N. Belk for initially suggesting the application of JSIM to this work. We would also like to thank Dr. J. Derov, Dr. S. Mittleman, and J. Moulton for assistance with the work done at Rome Laboratory.

*Present address: Dept. of Physics, U.S.M.A., West Point, NY.

[1] J. Halbritter, J. Supercond. **10**, 91 (1997).
[2] P. P. Nguyen, D. E. Oates, G. Dresselhaus, and M. S. Dresselhaus, Phys. Rev. B **48**, 6400 (1993).
[3] J. Halbritter, Phys. Rev. B **48**, 9735 (1993).
[4] T. L. Hylton, A. Kapitulnik, M. R. Beasley, J. P. Carini, L. Drabeck, and G. Grüner, Appl. Phys. Lett. **53**, 1343 (1988).
[5] T. L. Hylton and M. R. Beasley, Phys. Rev. B **39**, 9042 (1989).
[6] C. Attanasio, L. Maritato, and R. Vaglio, Phys. Rev. B **43**, 6128 (1991).
[7] L. R. Vale, R. H. Ono, and D. A. Rudman, IEEE Trans. Appl. Supercond. **7**, 3193 (1996).
[8] K. K. Likharev, *Dynamics of Josephson Junctions and Circuits* (Gordon and Breach, London, 1985).
[9] Y. M. Zhang, D. Winkler, P. A. Nilsson, and T. Cleason, Phys. Rev. B **51**, 8684 (1995).
[10] T. Ogawa and T. Yamashita, IEEE Trans. Appl. Supercond. **5**, 2204 (1995).
[11] D. E. Oates, P. P. Nguyen, Y. M. Habib, G. Dresselhaus, M. S. Dresselhaus, G. Koren, and E. Polturak, Appl. Phys. Lett. **68**, 705 (1996).
[12] Y. M. Habib, D. E. Oates, G. Dresselhaus, and M. S. Dresselhaus, IEEE Trans. Appl. Supercond. **7**, 2553 (1996).
[13] D. E. Oates, A. C. Anderson, and P. M. Mankiewich, J. Supercond. **3**, 251 (1990).
[14] D. M. Sheen, S. M. Ali, D. E. Oates, R. S. Withers, and J. A. Kong, IEEE Trans. Appl. Supercond. **AS-1**, 108 (1991).
[15] D. E. Oates, A. C. Anderson, D. M. Sheen, and S. M. Ali, IEEE Trans. Microwave Theory Tech. **39**, 1522 (1991).
[16] D. E. Oates, P. P. Nguyen, G. Dresselhaus, M. S. Dresselhaus, C. W. Lam, and S. M. Ali, J. Supercond. **5**, 361 (1992).
[17] M. Tinkham, *Introduction to Superconductivity* (McGraw-Hill, New York, 1996), pp. 213–224.
[18] A. Barone and G. Paterno, *Physics and Applications of the Josephson Effect* (Wiley, New York, 1982).

[19] A. M. Portis, J. Supercond. **5**, 319 (1992).
[20] D. M. Pozar, *Microwave Engineering* (Addison-Wesley, Reading, MA, 1990).
[21] E. S. Fang and T. van Duzer, *Extended Abstracts of the 1989 International Superconductivity Electronics Conference*, Tokyo, Japan (Japan Soc. Appl. Phys., Tokyo, Japan, 1989), p. 407.
[22] L. M. Xie, J. Wosik, and C. Wolfe, Phys. Rev. B **54**, 15 494 (1996).
[23] J. McDonald and J. R. Clem, Phys. Rev. B **56**, 14 723 (1997).
[24] J. McDonald, J. R. Clem, and D. E. Oates, Phys. Rev. B **55**, 11 823 (1997).
[25] D. E. Oates, Y. M. Habib, C. J. Lehner, J. Herd, R. Ono, and L. R. Vale, *Extended Abstracts of the 6th International Superconductive Electronics Conference (ISEC '97)*, Berlin, Germany (Physikalisch-Tehnische Bundesanstalt, Braunschweig, Germany, 1997), p. 77.
[26] J. S. Herd, D. E. Oates, and J. Halbritter, IEEE Trans. Appl. Supercond. **7**, 1299 (1997).